Dynamic Properties of the G93A Mutant of Copper−Zinc Superoxide Dismutase As Detected by NMR Spectroscopy: Implications for the Pathology of Familial Amyotrophic Lateral Sclerosis†

Eric L. Shipp,‡ Francesca Cantini,§ Ivano Bertini,§ Joan Selverstone Valentine,‡ and Lucia Banci*,§

Magnetic Resonance Center (CERM) and Department of Chemistry, University of Florence, Via Luigi Sacconi 6, 50019 Sesto Fiorentino, Italy, and Department of Chemistry and Biochemistry, University of California, Los Angeles, California 90095-1569

Received August 22, 2002; Revised Manuscript Received December 28, 2002

ABSTRACT: The backbone assignment of the copper−zinc superoxide dismutase amyotrophic lateral sclerosis G93A mutant was performed on an ^{15}N-enriched protein sample. ^{15}N R_1, R_2, and $R_{1\rho}$ and ^{15}N−^{1}H NOE experiments were then carried out at 600 MHz on G93A Cu_2Zn_2SOD and the values compared to the dynamics data for the "wild-type" protein. In addition, ^{15}N and ^{1}H chemical shift comparisons between wild-type Cu_2Zn_2SOD and its G93A mutant were also made. G93A exhibits a higher mobility than wild-type Cu_2Zn_2SOD, particularly in loops III and V, on a time scale faster than the rate of protein tumbling. There are also distinct chemical shift and NOE differences in residues 35−42 and 92−95, which comprise these loops. These two regions of Cu_2Zn_2SOD form the end of the β-barrel termed the "β-barrel plug" [Tainer, J. A., Getzoff, E. D., Beem, K. M., Richardson, J. S., and Richardson, D. C. (1982) *J. Mol. Biol. 160,* 181−217]. The increased mobility and reduction of the number of observed NOEs in this region indicate an opening of the β-barrel that may lead to amyloid fibrillogenesis. Alternatively, a motor neuron-specific substrate may bind this region of the protein, leading to deleterious modifications and/or reactions.

Amyotrophic lateral sclerosis (ALS)[1] is a progressive neurodegenerative disease that results in a gradual degradation of motor neurons in the motor cortex, brain stem, and spinal cord (*1*). A genetic link has been found in roughly 10% of all reported cases of the disease, which are collectively termed familial ALS (FALS). Of these cases, approximately one in five has been directly attributed to autosomal dominant mutations in the gene that encodes copper−zinc superoxide dismutase (Cu_2Zn_2SOD) (*2*−*5*). An intriguing aspect of these mutations is that they occur throughout the gene and yet in most instances do not significantly lower the SOD activity of the resulting enzyme (*6*).

At present, the mechanism or mechanisms whereby mutations in the gene encoding Cu_2Zn_2SOD cause the disease are unknown. A major insight into the role of Cu_2Zn_2SOD in FALS was gained when Gurney et al. found that transgenic mice expressing the FALS mutant G93A Cu_2Zn_2SOD developed progressive motor neuron disease despite having high levels of SOD activity (*7*). In addition, transgenic mice with no endogenous Cu_2Zn_2SOD were found not to develop motor neuron disease, suggesting that SOD-associated FALS is caused by a toxic gain of function induced by the ALS mutant Cu_2Zn_2SOD protein (*8*).

Cu_2Zn_2SOD is a 32 kDa homodimer containing two copper and two zinc ions per dimer (*9*). Reduction and oxidation of the copper ion mediates the disproportionation of superoxide anion to hydrogen peroxide and dioxygen ($2O_2^- + 2H^+ \rightarrow O_2 + H_2O_2$) (*10*). The tertiary structure of the enzyme is a Greek key β-barrel containing an internal disulfide bond (*11*, *12*), both of which contribute to its high stability, as characterized by its resistance to thermal denaturation as well as to proteolysis (*13*). It has been postulated that structural destabilization and/or an increase in mobility of Cu_2Zn_2SOD mutants may play a role in the pathology of Cu_2Zn_2SOD-related ALS (*14*−*17*). Conserved glycine residues are common in almost all of the known Cu_2Zn_2SOD proteins (*18*). Moreover, five missense mutations in the conserved glycine at residue 93 have been implicated in SOD-related FALS (*3*−*6*, *19*).

Numerous attempts were made to express and purify the most prominent Cu_2Zn_2SOD FALS mutant, A4V, prior to purifying G93A (unpublished work). The yield of the former mutant was much lower than for G93A. The A4V mutant experienced degradation, as found from ^{15}N-HSQC spectra

† This work was supported by European Community Contracts HPRI-CT-1999-00009 and HPRI-CT-1999-50018, by Italian CNR (Progetto Finalizzato Biotecnologie 01.00238.PF49), by COFIN 01 MIUR-ex 40%, and by Ente Cassa di Risparmio Firenze. We also gratefully acknowledge support from the ALS Association (Grant 20856) and the National Institutes of Health (Grants GM28222 and DK46828 to J.S.V. with a supplement to E.L.S.).

* To whom correspondence should be addressed: CERM and Department of Chemistry, University of Florence, Via L. Sacconi 6, 50019 Sesto Fiorentino, Italy. Telephone: +39 055 4574 263. Fax: +39 055 4574 253. E-mail: banci@cerm.unifi.it.

‡ University of California.

§ University of Florence.

[1] Abbreviations: ALS, amyotrophic lateral sclerosis; FALS, familial amyotrophic lateral sclerosis; Cu_2Zn_2SOD, copper−zinc superoxide dismutase; NOE, nuclear Overhauser effect; HSQC, heteronuclear single-quantum coherence; NOESY, nuclear Overhauser effect spectroscopy; CPMG, Carr−Purcell−Meiboom−Gill; R_1, longitudinal relaxation rate; R_2, transverse relaxation rate.

10.1021/bi026704y CCC: $25.00
Published on Web 01/29/2003

just 2−3 days after purification. These results are indicative of the inherent instability of the Cu_2Zn_2SOD FALS mutants at room temperature. Fortunately, G93A was stable enough that all the needed experiments in this study could be performed.

In the study presented here, the dynamic properties of the most prevalent of the G93X FALS mutants, G93A, are investigated by nuclear magnetic resonance spectroscopy and compared to those of the wild-type protein. As the aim of this study is to characterize the spectral and dynamical differences between the G93A mutant and wild-type Cu_2Zn_2SOD, we have performed the measurements with the same setup that was used for the already reported wild-type characterization (*17*). This is the first study of the dynamic properties of a Cu_2Zn_2SOD-related FALS mutant in which variations in mobility are characterized in distinct residues of the protein.

EXPERIMENTAL PROCEDURES

Sample Preparation. The human G93A Cu_2Zn_2SOD plasmid construct was created by PCR mutagenesis using the pPCuZnSOD1I^q plasmid (*20*) as a template. The template plasmid also contains the C6A and C111S mutations, which increase the thermostability of the sample and do not have discernible effects on the activity or the structure of Cu_2Zn_2SOD (*13*, *21*) (recombinant Cu_2Zn_2SOD with these two mutations is termed "wild type" in this paper). This is the same plasmid that was used for the earlier dynamics studies of wild-type Cu_2Zn_2SOD (*17*). After PCR mutagenesis, the resulting plasmid was sequenced and then expressed in the *Escherichia coli* TOPP1 (Stratagene) strain (*22*) to obtain the uniformly ^{15}N-labeled dimeric protein. The ^{15}N-enriched sample, termed G93A in this paper, was then isolated and purified according to a published procedure (*20*).

Protein purity was verified by ESI-mass spectrometry. The G93A Cu_2Zn_2SOD mutant was found to have 2.03 Cu and 2.3 Zn equivalents per dimer by inductively coupled plasma emission spectroscopy, which is consistent with a Cu_2Zn_2SOD holoenzyme. Differential scanning calorimetry was also performed as previously described to ensure sample homogeneity (*15*). Protein concentrations were determined by UV spectroscopy using a molar extinction coefficient of 1.08×10^4 M^{-1} cm^{-1} at 280 nm for the purified enzyme. The final protein sample, at a concentration of 2.5 mM in 20 mM phosphate (pH 5.0), was reduced with 5−7 mM isoascorbate and loaded into an NMR tube in a VacAtmosphere chamber under nitrogen at 12 °C.

NMR Spectroscopy. The NMR experiments for the backbone assignment were carried out at 298 K on a Bruker Avance spectrometer operating at 700 MHz. Two-dimensional (2D) ^{15}N-HSQC, 2D NOESY, three-dimensional (3D) ^{15}N-NOESY-HSQC, and HNHA experiments were performed to obtain the backbone assignments. The two-dimensional NOESY spectrum was recorded with a spectral width of (^{1}H) 18 250 Hz × (^{1}H) 18 250 Hz, using (^{1}H) 2048 × (^{1}H) 896 data points. The three-dimensional ^{15}N-NOESY-HSQC and HNHA spectra were both collected with (^{1}H) 10 504 Hz × (^{15}N) 2980 Hz × (^{1}H) 10 504 Hz as the spectral window. There were (^{1}H) 1024 × (^{15}N) 56 × (^{1}H) 400 and (^{1}H) 1024 × (^{15}N) 36 × (^{1}H) 200 data points, respectively. All mobility NMR experiments were carried out at 298 K on a Bruker Avance spectrometer operating at 600 MHz. This spectrometer contained a triple-resonance (TXI) 5 mm probe equipped with pulsed field gradients (PFG) along the *z*-axis. In this study, all the relaxation measurements were collected with the same procedures used for the wild-type Cu_2Zn_2SOD (*17*) to ensure meaningful comparison between the two sets of data and avoid systematic errors. R_1, R_2, and heteronuclear NOEs were measured with the gradient-enhanced, sensitivity-enhanced pulse sequences as described by Farrow et al. (*23*). Constant temperature throughout the acquisition of data was maintained by the application of temperature compensation methods (*24*); possible shift variations were minimized by interleaving experiments with different delays (*25*). The ^{15}N longitudinal relaxation rates (R_1) were measured with delays of 2.5, 35, 75, 270, 400, 650, 750, 1000, 1750, 2500, and 3000 ms. The ^{15}N transverse relaxation rates (R_2) were measured using a CPMG sequence (*26*) with delays of 9.8, 19.5, 29.3, 39.0, 48.4, 58.6, 68.3, 78.1, 87.8, 97.7, 107.4, and 117.1 ms and a refocusing time (τ_{CPMG}) of 225 μs. In both R_1 and R_2 measurements, the first delay was duplicated. A recycle delay of 3 s was used for R_1, R_2, and heteronuclear NOEs without proton saturation measurements. In the heteronuclear NOE experiment with proton saturation, the latter was achieved with a train of 120° ^{1}H pulses at 5 ms intervals applied for 3 s. All experiments utilized the "water flipback" suppression scheme to minimize the saturation of water by orienting it along the +*z*-axis during acquisition (*27*). All 2D data consisted of 2K data points in the acquisition dimension and of 256 experiments in the indirect dimension with eight scans and spectral widths of 8928 (^{1}H) and 2553 Hz (^{15}N).

To monitor contributions to transverse relaxation from exchange processes, the R_2 values of the ^{15}N nuclei were also measured as a function of τ_{CPMG} (*26*, *28*). Sets of experiments were carried out at six τ_{CPMG} values: 225, 350, 450, 575, 700, and 1000 μs. Relaxation delays varied from 9 to 120 ms, with the exact values depending on τ_{CPMG}.

The ^{15}N off-resonance rotating-frame relaxation rates ($R_{1\rho}^{OFF}$) were measured as a function of the effective magnetic field amplitude (ω_{eff}) using a previously reported pulse sequence (*29*). ω_{eff} was modulated by changing both the ω_1 frequency and amplitude which has an offset ($\Delta\omega$) with respect to the center of the amide nitrogen resonances. This determines the effective magnetic field amplitude ω_{eff} [$=(\Delta\omega^2 + \omega_1^2)^{1/2}$], which makes an angle of θ [$=\arctan(\omega_1/\Delta\omega)$] with the *y*-axis of the ^{15}N magnetization. The ω_1 amplitude was increased and decreased gradually in a trapezoidal fashion to achieve adiabatic rotation of the magnetization to the effective magnetic field axis (*30*). For each ω_1 amplitude value, a series of 2D experiments were performed in which the relaxation delays were set to range from 10 to 200 ms.

Data Analysis. Relaxation rates R_1, $R_{1\rho}^{OFF}$, and R_2 were determined by fitting the cross-peak intensities (I), measured as a function of the delay (T) within the pulse sequence, to a single-exponential decay curve using the Levenburg−Marquardt algorithm (*31*, *32*) according to the following equation:

$$I(T) = I_0[\exp(-RT)] \quad (1)$$

where I_0 and R are the adjustable fitting parameters. The

use of a two-parameter fitting reflects the setup of the experiments (the properties of the pulse sequences) where the magnetization tends to 0 at infinite delay. Examples of ^{15}N R_1 and R_2 data recorded for G93A Cu_2Zn_2SOD are reported in Figure 1 of the Supporting Information. The errors on the relaxation parameters were estimated through a Monte Carlo approach by fitting 500 simulated data sets (*33*) generated from the optimized parameters with the addition of a Gaussian noise of standard deviation equal to either 5% of the largest peak intensity or the semidispersion of the intensities in replicated experiments.

The heteronuclear ^{1}H−^{15}N NOE values were measured by considering the ratio of the peak volumes in spectra recorded with and without ^{1}H saturation. Two duplicate spectra were analyzed in a similar way to derive the uncertainty of the measurements.

Rotating Frame Relaxation Rates. Rate $R_{1\rho}$ of a ^{15}N spin, measured applying an off-resonance ω_{eff} ($R_{1\rho}^{\mathrm{OFF}}$), is related to relaxation and exchange parameters by the following expression (*34*, *35*):

$$R_{1\rho}^{\mathrm{OFF}} = R_1 \cos^2\theta + R_{1\rho}^{\mathrm{ON},\infty} \sin^2\theta + K \sin^2\theta \frac{\tau_{\mathrm{ex}}}{1 + \tau_{\mathrm{ex}}^2 \omega_{\mathrm{eff}}^2} \quad (2)$$

where R_1 is the longitudinal relaxation rate, $R_{1\rho}^{\mathrm{ON},\infty}$ is the on-resonance rotating frame relaxation rate with an infinitely large effective field amplitude, and τ_{ex} is the correlation time for the exchange process for the spin under observation. K is a constant equal to $p_a p_b \delta\Omega^2$, where p_a and p_b are the relative populations of the two states, a and b, between which the exchange process occurs and $\delta\Omega$ is the chemical shift difference of the resonating nucleus between these two states. Equation 2 is valid when $\delta\Omega\tau_{\mathrm{ex}} \ll 1$ and off-resonance effects are neglected (*36*).

To compare the $R_{1\rho}$ values measured with different ω_{eff} values, $R_{1\rho}^{\mathrm{OFF}}$ should be corrected to take into account the different θ angles (*29*):

$$R_{1\rho}^{\mathrm{OFF,cor}} = \frac{R_{1\rho}^{\mathrm{OFF}} - R_1 \cos^2\theta}{\sin^2\theta} = R_{1\rho}^{\mathrm{ON},\infty} + \mathrm{K}\frac{\tau_{\mathrm{ex}}}{1 + \tau_{\mathrm{ex}}^2 \omega_{\mathrm{eff}}^2} \quad (3)$$

In the measurements presented here, ω_{eff} varied between $880 \times 2\pi$ and $2200 \times 2\pi$ s^{-1}, thus setting the range of the exchange process rates (τ_{ex}^{-1}) from 7×10^3 to 2×10^4 s^{-1}, the dependence of which can be detected in these experiments.

CPMG Spin-Echo Pulse Train. In the R_2 measurements with the CPMG sequence, the contributions to transverse relaxation due to exchange processes are related to the τ_{CPMG} length by the following equations:

$$R_{\mathrm{ex}} = \frac{K_{\mathrm{ex}}}{2} - 2\nu_{\mathrm{eff}} \sinh^{-1}\left(\frac{K_{\mathrm{ex}}}{\xi}\sinh\frac{\xi}{4\nu_{\mathrm{eff}}}\right) \quad (4)$$

$$\nu_{\mathrm{eff}} = \frac{1}{2(T_\pi + \tau_{\mathrm{CMPG}})} \quad (5)$$

where $\xi = (K_{\mathrm{ex}}^2 - 4p_a p_b \delta\Omega^2)^{1/2}$, $K_{\mathrm{ex}} = 1/\tau_{\mathrm{ex}}$, and T_π is the duration of a 180° ^{15}N CPMG pulse. When τ_{ex} is longer than τ_{CPMG}, no effect due to conformational exchange processes is observed. Experimental limits on the spin-echo delay length are determined by the duty cycle of the transmitter for short delays and the evolution of ^{1}H−^{15}N coupling during long delays. In this study, ν_{eff} ranges between 400 and 1600 s^{-1} which sets the limits for the detection of the frequency dependence of R_2 to 2.5×10^3 to 1×10^4 s^{-1}.

Model-Free Analysis. The experimental longitudinal and transverse relaxation rates and the heteronuclear NOEs have been analyzed with the Model-Free approach, proposed by Lipari and Szabo (*37*), and its subsequently extended version proposed by Clore et al. (*38*).

The equations for the relaxation rates, in terms of spectral density functions [$J(\omega)$], are well-known (*39*). Within the Model-Free analysis, the relaxation rates are expressed as a function of the overall rotational correlation time τ_{m}, the generalized order parameter S^2, and the correlation time for internal motions, which can be considered to arise from two components, one describing faster (τ_{f}) and one slower (τ_{s}) motions (collectively called τ_{e}), but always faster than τ_{m}. To ensure proper fitting of R_2, the Model-Free program also takes into account a contribution from exchange processes (R_{ex}) when necessary.

The generalized order parameter S^2 characterizes the amplitude of internal motions of the ^{1}H−^{15}N vector in each residue. A value of 1 indicates complete internal restriction of the ^{1}H−^{15}N bond, whereas a value of 0 represents no internal restriction.

Following a well-established procedure (*38*) initially, the relaxation rates are analyzed in terms of spectral densities, which, in the simplest case and for isotropic tumbling, is

$$J(\omega) = {}^2/_5\left[\frac{S^2\tau_{\mathrm{m}}}{1 + (\omega\tau_{\mathrm{m}})^2}\right] \quad (6)$$

where the only variable parameter is S^2, τ_{m} being the overall rotational correlation time (model 1).

An *F*-statistic test (*40*) can be applied to evaluate the quality of the fitting with respect to the model used for data analysis. When the fitting using eq 6 is poor, a second term is added to the spectral density function, according to the following equation:

$$J(\omega) = {}^2/_5\left[\frac{S^2\tau_{\mathrm{m}}}{1 + (\omega\tau_{\mathrm{m}})^2} + \frac{(1 - S^2)\tau'}{1 + (\omega\tau')^2}\right] \quad (7)$$

where $\tau'^{-1} = \tau_{\mathrm{m}}^{-1} + \tau_{\mathrm{e}}^{-1}$ and τ_{e} is the correlation time for internal motions faster than τ_{m} (model 2).

When internal motions of significant amplitude occur on two different time scales, but still faster than τ_{m}, the Model-Free spectral density function extends to

$$J(\omega) = {}^2/_5\left[\frac{S^2\tau_{\mathrm{m}}}{1 + (\omega\tau_{\mathrm{m}})^2} + \frac{(S_{\mathrm{f}}^2 - S^2)\tau'_{\mathrm{s}}}{1 + (\omega\tau'_{\mathrm{s}})^2} + \frac{(1 - S_{\mathrm{f}}^2)\tau'_{\mathrm{f}}}{1 + (\omega\tau'_{\mathrm{f}})^2}\right] \quad (8)$$

where the slow and fast motions have different correlation times (τ_{s} and τ_{f}), $\tau'^{-1}_{\mathrm{s}} = \tau_{\mathrm{m}}^{-1} + \tau_{\mathrm{s}}^{-1}$ and $\tau'^{-1}_{\mathrm{f}} = \tau_{\mathrm{m}}^{-1} + \tau_{\mathrm{f}}^{-1}$, S^2 ($=S_{\mathrm{f}}^2 S_{\mathrm{s}}^2$) is the square of the generalized order parameter characterizing the amplitude of the internal motions, and S_{f}^2

and S_s^2 are the squares of the order parameters for the internal motions on the fast and slow time scales, respectively.

Since the number of parameters usually exceeds the number of experimentally accessible data, it is commonly assumed that $\tau_f < 20$ ps. The third term of eq 8 is then sufficiently small that it makes a negligible contribution to the relaxation parameters (*38*, *41*) and simplifies eq 8 to

$$J(\omega) = {}^2/_5\left[\frac{S^2\tau_m}{1+(\omega\tau_m)^2} + \frac{(S_f^2 - S^2)\tau_s'}{1+(\omega\tau_s')^2}\right] \quad (9)$$

to fit the data (model 5).

When the overall motion is axially symmetric (*42*), τ_m^{-1} assumes the following values: $\tau_{m1}^{-1} = 6D_\perp$, $\tau_{m2}^{-1} = 5D_\perp + D_{||}$, $\tau_{m3}^{-1} = 2D_\perp + 4D_{||}$. Consequently, the spectral densities of eqs 6−9 become a summation over three components of the diffusion tensor. The three terms of the summation are multiplied by A_1 [$=(3\cos^2\theta - 1)^2/4$], A_2 ($=3\sin^2\theta\cos^2\theta$), and A_3 ($={}^3/_4\sin^4\theta$), respectively, where θ is the angle between the H−N bond vector and the unique axis of the principal frame of the diffusion tensor (*43*).

The rotational diffusion tensor (D) and the initial τ_m values were estimated from the R_2/R_1 ratio with the program Quadric Diffusion (*43*, *44*). Once the best model for the molecular motions was selected on the basis of an F-statistic test (*40*) of the Model-Free analysis, the overall τ_m, the $D_{||}/D_\perp$ ratio, and the internal motion parameters for each spin were optimized by fitting the experimental relaxation data (R_1, R_2, and NOE) using the Powell minimization algorithm (*35*). In this analysis, an axially symmetric model was used to account for the global rotational motion of the protein.

Estimation of Conformational Entropy from NMR Relaxation Data. Order parameters (S^2) are related to conformational entropy (S_{conf}) because they indicate the range of structural states accessible to a bond vector (*45*). It has been previously shown that, in the assumption that the motions of the individual bond vectors are independent, an upper limit (in magnitude) of the entropy changes occurring between two states of a protein can be calculated from order parameters (*46*):

$$\Delta S/k_b = \ln\lfloor[3 - (1 + 8S_{n,2})^{1/2}]/[3 - (1 + 8S_{n,1})^{1/2}]\rfloor \quad (10)$$

where S is the conformational entropy, k_b is Boltzmann's constant, and S_n are the order parameters of the nth H−N vectors in the two states. In this specific case, the initial state (state 1) is the wild-type Cu_2Zn_2SOD and the final state (state 2) is the G93A Cu_2Zn_2SOD mutant.

RESULTS

Resonance Assignment of G93A Cu_2Zn_2SOD. The G93A Cu_2Zn_2SOD mutant exhibits a well-dispersed and well-resolved ^{15}N-HSQC spectrum indicative of a folded protein. However, this mutant, particularly at the concentrations needed for NMR characterization (around 1 mM), is unstable and after ~2 weeks at room temperature starts to denature and eventually becomes completely unfolded. This prevents us from performing a more extensive spectral characterization. Nevertheless, we have been able to assign its spectrum and to study its dynamical properties. The backbone assignment was aided by using the automatic assignment program

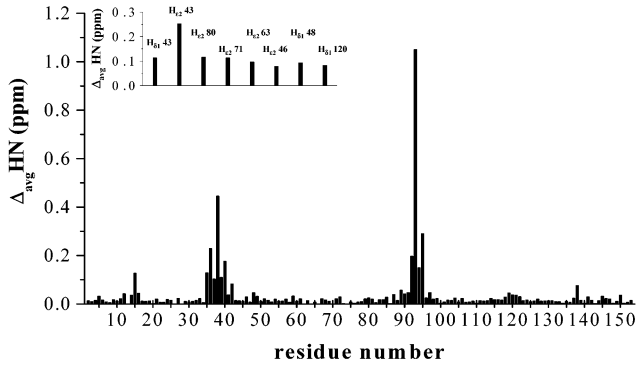

FIGURE 1: HN chemical shift differences between wild-type and G93A Cu_2Zn_2SOD. The weighted average differences (Δ_{avg}HN) in chemical shift are determined as $\{[(\Delta H)^2 + (\Delta N/5)^2]/2\}^{1/2}$, where ΔH and ΔN are chemical shift differences for ^{1}H and ^{15}N, respectively (*61*). The inset reports the Δ_{avg}HN values for the HN groups of the histidine ring.

GARANT (*47*) run on a Linux processor cluster. The peak lists of ^{15}N-NOESY-HSQC and ^{15}N-HSQC experiments, as well as the solution structure of the Cu_2Zn_2SOD dimeric protein (*48*), were used as input for the program. Of the 147 expected cross-peaks in the ^{15}N-HSQC spectrum, only Phe64 and Lys70 could not be assigned. The ^{15}N-HSQC spectrum of G93A Cu_2Zn_2SOD was nearly identical to that of the wild-type protein (*48*), indicating structural similarity between the two, with the exception of a few areas of localized variations in chemical shift (Figure 1). These areas are very well-defined, being limited to segments of residues 14−16, 35−41, and 89−95. Furthermore, the NOE patterns observed from the ^{15}N-NOESY-HSQC spectra were virtually equal for all residues except for those experiencing variations in chemical shift with respect to the wild type. A number of residues located in the segments of residues 35−40 and 90−95 show a sizable reduction in the number and intensities of NOE cross-peaks.

Relaxation Measurements. The backbone NH dynamics of G93A Cu_2Zn_2SOD were investigated on both the millisecond to microsecond and nanosecond to picosecond time scales. The G93A Cu_2Zn_2SOD relaxation measurements were carried out under the same sample and experimental conditions that were used for the wild-type Cu_2Zn_2SOD (*17*) to avoid systematic errors between the two sets of data. We obtained reliable R_1, R_2, and NOE data for 138 of the possible 145 residues that contain backbone NH groups. Glu40, Asn53, Ser59, Ser68, Val118, His120, and Asn131 could not be analyzed due to peak overlap or an inadequate peak signal/noise ratio.

The average R_1, R_2, and NOE values for G93A Cu_2Zn_2SOD were 0.62 ± 0.06 s^{-1}, 30.1 ± 3.4 s^{-1}, and 0.83 ± 0.12, respectively. The experimental data are reported in Figure 2 of the Supporting Information. The average R_1, R_2, and NOE values for wild-type Cu_2Zn_2SOD are 0.60 ± 0.11 s^{-1}, 33.9 ± 4.1 s^{-1}, and 0.81 ± 0.10, respectively (*17*).

The residues that exhibit conformational exchange processes from CPMG and $R_{1\rho}$ analysis in G93A Cu_2Zn_2SOD are Val7, Asn19, Gln22, Lys30, Gly37, Phe45, His48, Cys57, Val81, Ala95, Leu117, Lys122, Thr137, and Gly147. Furthermore, residues Phe20, Asp52, and Ser107 have R_2 values higher than the average, indicating the presence of exchange processes occurring in less than 50 μs. In wild-type

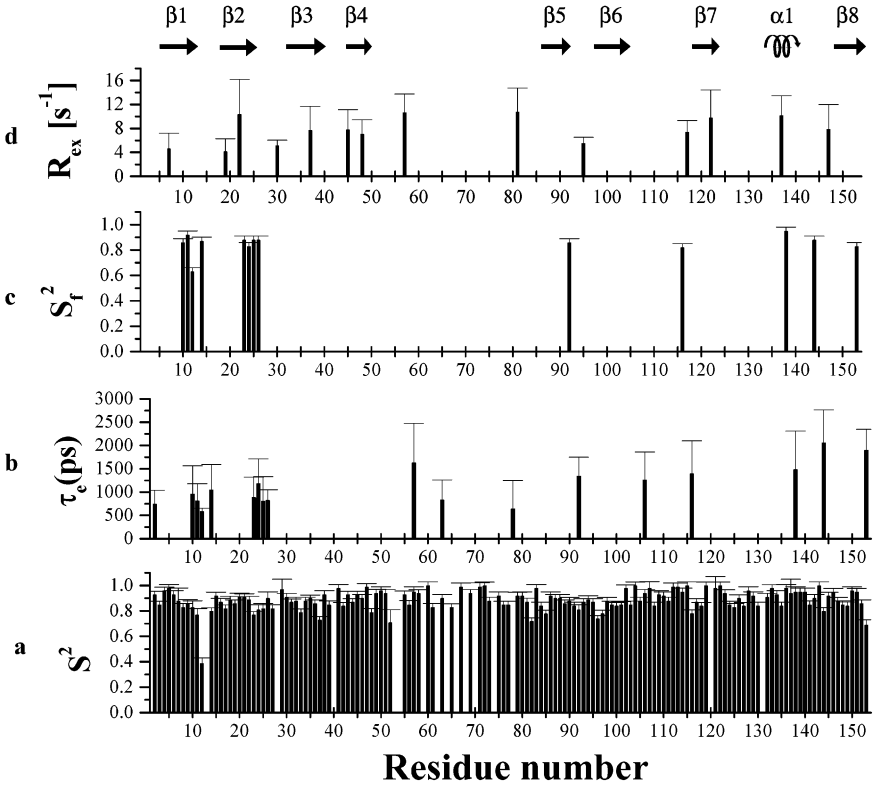

FIGURE 2: Model-Free parameters of G93A Cu_2Zn_2SOD. Shown are backbone amide order parameters S^2 (a), the effective correlation time for these fast motions (τ_e) (b), the order parameters for the fast motions (S_f^2) (c), and the conformational exchange contribution to R_2 as determined from CPMG and $R_{1\rho}$ analysis as a function of residue number. The secondary structure elements are reported at the top.

Cu_2Zn_2SOD, the residues that exhibit conformational exchange processes from $R_{1\rho}$ analysis are Asn19, Phe20, Thr54, Cys57, Thr58, Ser107, Leu117, Lys122, Leu126, Ala145, and Ile151 (*16*). Residue Gly127 has an R_2 value that is higher than the average.

Analysis of the Relaxation Data. Within the Model-Free analysis, the crystal structure of the G37R mutant of human Cu_2Zn_2SOD (*16*) was used to calculate the inertia tensor as was done for the wild-type Cu_2Zn_2SOD (*17*). The relaxation data are best fit by an axial diffusion tensor with the $D_{||}/D_{\perp}$ ratio equal to 1.26 ± 0.06. The same value is also found if the solution structure of wild-type Cu_2Zn_2SOD (*48*) is used. For wild-type Cu_2Zn_2SOD, the $D_{||}/D_{\perp}$ ratio was found to be 1.24 ± 0.02, which is essentially equal to that of the mutant described here. The τ_m value obtained from the fitting of the relaxation data for G93A Cu_2Zn_2SOD is 22.9 ± 1.6 ns which compares well with a value of 25.3 ± 2.1 ns for wild-type Cu_2Zn_2SOD (*17*).

The average S^2 value is 0.89 ± 0.04 (Figure 2a) which is comparable to the average S^2 value obtained for wild-type Cu_2Zn_2SOD of 0.92 ± 0.04 (*17*). Most of the residues are fitted using S^2 as the only variable parameter (model 1). Values for the effective internal correlation time τ_e can be determined for 18 residues (Figure 2b), all located in the loop regions. Some of the latter residues are better described with two classes of internal motions (model 5), and the order parameter (S_f^2) for the fast internal motions can be determined (Figure 2c). The latter residues are mainly located at the N-terminus of the protein and are all clustered in two loop regions experiencing collective motions, with some scattered residues throughout the length of the protein (residues 116 and 138).

Conformational exchange contributions to R_2 from Model-Free analysis (R_{ex}) were found for Phe20, Asp52, Ser107, and Thr137, consistent with their R_2 values being higher than the average. The relaxation parameters of residues Thr54, Ser68, and Glu78 cannot be fitted within the Model-Free analysis.

DISCUSSION

The structure of G93A Cu_2Zn_2SOD is very similar to that of wild-type Cu_2Zn_2SOD since the ^{15}N-HSQC spectra and NOE patterns of the two proteins are nearly identical with the exception of two distinct segments (residues 35−42 and 92−95) shown in Figure 1. These two areas showing ^{15}N and ^{1}H chemical shift differences between wild-type and G93A Cu_2Zn_2SOD involve loops III and V. The shift differences are appreciable enough to indicate local structural variations in these two regions of the protein. It is clear that the disruption of local interactions between these two conserved areas induced by the mutation alters the local structure as well as enhances the backbone mobility in these loops. The differences in chemical shifts found in these regions correlate well with the observation that electrostatic and hydrophobic interactions between these two regions significantly contribute to the stability of the β-barrel structure of Cu_2Zn_2SOD (*11*, *12*, *16*, *48*). There is also a slight chemical shift difference for Gln15 in G93A Cu_2Zn_2SOD when compared to the wild type, indicating a structural rearrangement in the area near Val14 which stabilizes loop III by interacting with Leu38 (*16*). Moreover, His43 Hϵ_1, which is involved in hydrogen bonding to the carbonyl oxygen of residues 39 and 40 (*48*), is shifted considerably

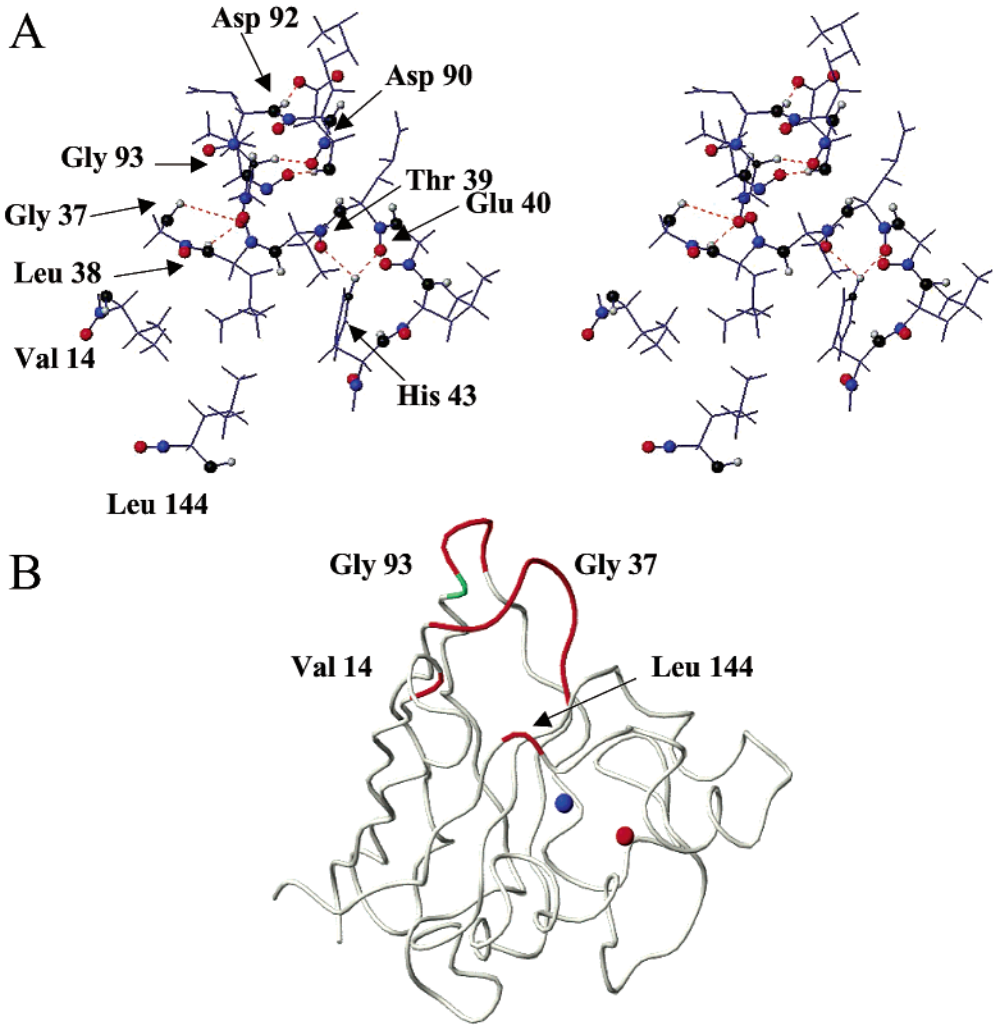

FIGURE 3: Hydrogen bond network in the β-barrel plug of Cu_2Zn_2SOD. The hydrogen bond network is taken from the solution structure of Cu_2Zn_2SOD (*48*). The residues that comprise the β-barrel plug (*3*, *12*) are depicted in panel A. Carbon is shown in blue, oxygen in red, nitrogen in black, and hydrogen in gray. The hydrogen bonds are represented as orange dashed lines. (B) The ribbon diagram highlights the protein structure of the region shown in panel A. The green segment indicates Gly93.

in G93A Cu_2Zn_2SOD relative to the wild type (Figure 1, inset).

The average backbone S^2 value for the G93A Cu_2Zn_2SOD mutant is 0.89 ± 0.04, indicating an essentially rigid protein. S^2 values in this range are typically seen in proteins such as Cu_2Zn_2SOD that contain a large amount of β-strands in their secondary structures (*17*, *49*, *50*). Most of the residues of G93A Cu_2Zn_2SOD located in the β-strands, with the exception of strand β6 which follows the G93A mutation (residues 94−101), have high S^2 values indicating high rigidity of the protein (Figure 2a).

The G93A mutation occurs in loop V of Cu_2Zn_2SOD and is in an area of the protein in which hydrogen bonding interactions are thought to facilitate the "plug" end of the β-barrel (*3*, *48*). In addition, there is evidence to suggest that the presence of the left-handed Gly93 residue is critical in maintaining packing interactions in this area of the protein (*51*). Therefore, it is not surprising that residues around the mutation experience sizable internal mobility. Strand β6 is also significantly more mobile in the mutant than in wild-type Cu_2Zn_2SOD (average S^2 of 0.93 ± 0.04 in the wild type vs 0.84 ± 0.03 in the mutant). This may be also a result of the disruption of the hydrogen bond network in loop V due to the mutation. The hydrogen bond network around Gly93 found in the solution structure of human Cu_2Zn_2SOD is shown in Figure 3 (*48*). Hydrogen bonds between the Asp92−Asp90, Asp90−Val94, and Gly93−Asp90 pairs aid in stabilizing the turn in loop V (*11*, *16*, *48*, *52*). This decrease in rigidity may play a role in the in vivo instability previously found in G93C, another ALS mutant with a substitution at residue 93 (*6*).

Contrary to the behavior of β-strands, residues located in loops are characterized by S^2 values that are lower than the average (Figure 2a). Particularly striking is the very low S^2 value of Gly12 (0.39 ± 0.04) which is located in loop I. Interestingly, the residues around the electrostatic channel (loop VII) in G93A Cu_2Zn_2SOD do not exhibit internal mobility. This area is instead characterized by large S^2 values.

Values for the internal correlation internal time (τ_e) and fast order parameter (S_f^2) are found for residues clustered in two loop regions, and these regions experience collective motions (Figure 2b,c). This is expected since loop regions normally display greater mobility than residues involved in secondary structural elements. Conformational exchange processes are involving residues scattered along the protein

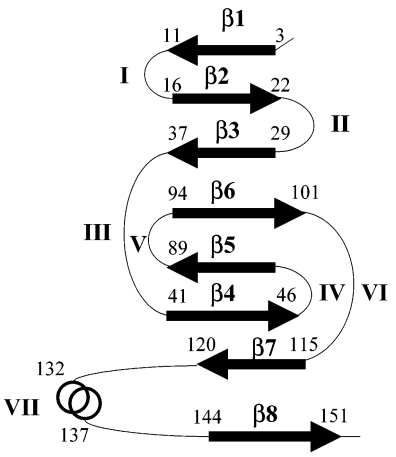

FIGURE 4: Cu_2Zn_2SOD secondary structure. β-strands, as found in the solution structure of wild-type Cu_2Zn_2SOD (*48*), are numbered beginning from the N-terminus of the protein and loop regions are designated by Roman numerals.

backbone that are present both in the long loop IV and in several β-strands.

Comparison of the Backbone Dynamics and NMR Parameters of G93A and Wild-Type Cu_2Zn_2SOD. To compare the backbone mobilities of the G93A Cu_2Zn_2SOD mutant and wild-type Cu_2Zn_2SOD, the differences in S^2 values for both proteins are displayed in Figure 5. A positive value indicates that the H−N vector is more rigid in wild-type Cu_2Zn_2SOD than in G93A Cu_2Zn_2SOD, whereas a negative value indicates the opposite. Interestingly, the G93A Cu_2Zn_2SOD protein appears to be more mobile than the wild type, which is characterized by an overall average S^2 value of 0.92 ± 0.04, at many residues located throughout the protein. The most notable differences in S^2 are observed for residues 10−17, 35−37, 76−84, 92−103, 117, 127, 144, 148, and the final two C-terminal residues, which are depicted in Figure 6. Interestingly, the residues in the electrostatic channel (loop VII) do not experience an appreciable difference in mobility relative to the wild type. This result seemingly rules out the possibility that a large molecule binds nonspecifically to the copper site as a consequence of increased flexibility around the electrostatic channel. However, the increased overall dynamics of the mutant protein may still provide increased access of small molecules, such as H_2O_2 or peroxynitrite, to the copper site, resulting in potentially toxic free radical chemistry (*53*, *54*).

The packing interactions found between Val14, residues 35−38, and Leu144 also contribute to the formation of the β-barrel plug (*3*, *48*) (Figure 3). These residues were also found to exhibit more mobility than the wild type. These findings strengthen the idea that the substitution of glycine with alanine at position 93 disrupts the normal hydrogen bond network and renders G93A Cu_2Zn_2SOD more mobile than the wild type in a global as well as local sense.

Another region of G93A Cu_2Zn_2SOD that has S^2 values significantly lower than those reported for the wild-type protein is the segment between residues 76 and 84, with average S^2 values of 0.86 ± 0.03 in the mutant and 0.95 ± 0.03 in the wild type. These residues comprise roughly half of the zinc subloop and contain two of the zinc binding ligands. This enhanced flexibility at the zinc site is not due to the absence of zinc since the G93A Cu_2Zn_2SOD sample studied here was found to be fully metalated with two copper and two zinc ions per protein dimer (see Experimental Procedures). Moreover, to our knowledge, there is no evidence that indicates a zinc deficiency in vivo in the majority of FALS mutant Cu_2Zn_2SOD proteins (*14*, *55*). Nevertheless, previous studies on the zinc binding properties of isolated Cu_2Zn_2SOD-related FALS mutants do suggest that the zinc sites of these proteins are altered in some fashion (*56*, *57*). The enhanced mobility in this region may be related to these altered binding properties of the zinc site in the FALS mutant proteins.

Surprisingly, there are a number of residues in the wild-type protein with S^2 values lower than those observed in G93A Cu_2Zn_2SOD (Figure 5). The residues also display conformational exchange processes in the wild type with the exception of Gly108 (*17*), whereas they do not in the mutant. Two of these residues, Ala89 and Val94 which are spatially close to each other, may be stabilized in the mutant via hydrophobic interactions. Since Asp90, Lys91, Asp92, and Ala93 are more flexible due to the mutation, it is reasonable to assume that Ala89 and Val94 might be closer in space and thereby positioned within the van der Waals radius of interaction. Perhaps long-range effects induced by the increased mobility around the β-barrel plug (*3*) create steric constraints around these residues, consequently rendering them less mobile.

The differences in mobility (in terms of S^2) between two species are related to their differences in entropy (ΔS) via eq 10. The validity of this equation is limited to residues with S^2 values of <0.95 (*46*). If residues with a value of S^2 higher than this limit are excluded, the entropy difference between G93A and wild-type Cu_2Zn_2SOD is estimated to be 40 ± 13 J mol^{-1} K^{-1}. This value indicates a global higher disorder in G93A Cu_2Zn_2SOD. However, entropy variations calculated from order parameters should not be taken as the total entropic difference since the former contribution reflects only differences in rapid motions detected by NMR. Of course, additional factors are expected to contribute to the total entropy difference.

The medium- and long-range NOEs observed in the wild-type protein between residues in loops I, III, and V and in strand β6 are either not present or dramatically decreased in intensity in G93A Cu_2Zn_2SOD. This observation directly correlates with the increased internal mobility in the mutant.

Biological Implications of the G93A Mutation. Mice expressing Cu_2Zn_2SOD mutants have been seen to contain intracellular plaques or inclusions in their motor neurons, most of which occur before the onset of the phenotypic observations associated with ALS (*58*). In particular, spinal cords of mice expressing G93A were found to contain insoluble high-molecular weight complexes composed of G93A (*59*). These data suggest a tendency of Cu_2Zn_2SOD mutants to aggregate due to the decreased stability of the protein. Although G93A was found to be similar in terms of thermal stability to the wild type (data not shown), over time it shows a slow denaturation which might be linked to the increased mobility in many areas of the protein. Moreover, recent structural analysis suggests that β-barrel folds have continuous hydrogen bond networks around the ends of the β-cylinder to protect proteins from aggregation arising from edge-to-edge contacts between neighboring β-sheet proteins (*60*). The loss of hydrogen bonding around

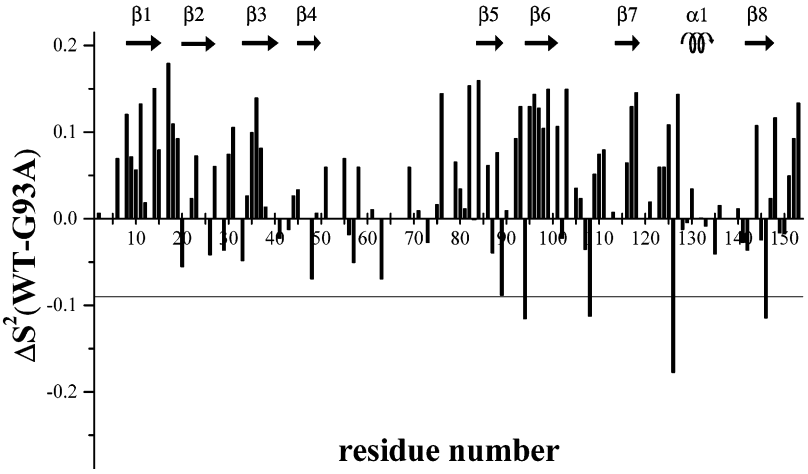

FIGURE 5: Differences in order parameters between wild-type and G93A Cu_2Zn_2SOD. A positive value indicates that the H−N vector is more rigid in wild-type Cu_2Zn_2SOD than in G93A Cu_2Zn_2SOD, whereas a negative value indicates the opposite. The two thin lines represent the sum of the average errors from fitting. The secondary structure elements are reported at the top.

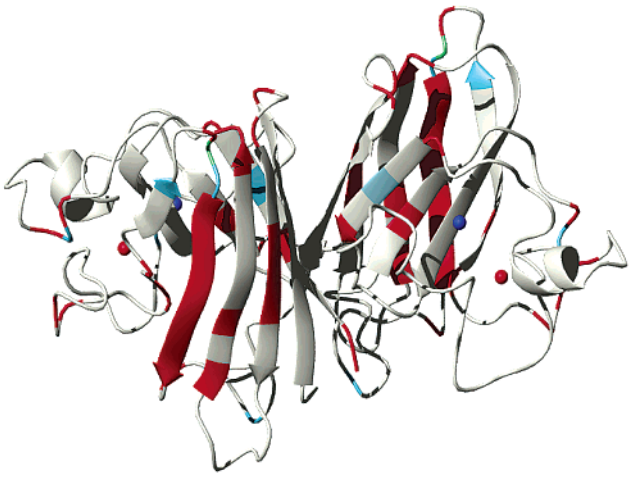

FIGURE 6: Differences in internal mobility between wild-type and G93A Cu_2Zn_2SOD in S^2. The solution structure of Cu_2Zn_2SOD (*48*) was used to illustrate the areas with markedly different S^2 values between the two systems. Only residues with S^2 values differing by more than ±0.09 (sum of the error) are colored. Red depicts residues in G93A Cu_2Zn_2SOD with a lower and blue with a higher order parameter than wild-type Cu_2Zn_2SOD. Green indicates the position of the G93A mutation.

the β-barrel plug as well as the increase in NH mobility, observed in G93A, might favor edge-to-edge aggregation and β-sheet amyloid fibrillogenesis (*60*).

The large number of Cu_2Zn_2SOD-related FALS mutations at residue 93 indicates that the loss of the glycine and not the addition of an alanine is an important factor in the pathology arising from G93A Cu_2Zn_2SOD. The loss of rotational degrees of freedom brought about by replacing the glycine increases the mobility of the residues surrounding the mutation. This resulting increase in mobility may create a dynamic transient opening in the β-barrel plug of G93A Cu_2Zn_2SOD that contains dissimilar electrostatic characteristics with respect to the active site channel, subsequently allowing small molecules to bind the protein and possibly facilitating G93A aggregation. Either a combination of edge-to-edge interactions, aberrant ligand binding, or both may explain the motor neuron-specific aggregation of Cu_2Zn_2-SOD observed in FALS transgenic mice (*59*). The enhanced mobility of strand β6 immediately following the G93A Cu_2Zn_2SOD mutation may also aid in the creation of such a binding site. It is conceivable that the creation of an aberrant binding site in G93A Cu_2Zn_2SOD may aid in bringing about the toxic properties associated with Cu_2Zn_2SOD FALS mutants.

In this study, we have found that G93A Cu_2Zn_2SOD displays enhanced backbone mobility relative to wild-type Cu_2Zn_2SOD on the nanosecond to picosecond time scale stemming from the loss of important interactions between residues that comprise the β-barrel plug (*3*, *48*). Chemical shift analysis and NOE analysis have also revealed structural differences between the residues involved in this region. There are also a number of other Cu_2Zn_2SOD-related FALS mutations located in this critical area such as G37R, L38V, L38R, H43R, A89V, D90A, and D90V (up to date list of ALS mutations available at www.alsod.org). The G37R Cu_2Zn_2SOD mutant is also thought to be flexible in this region as indicated by the presence of high atomic displacement parameters in the crystal structure (*16*). Because of the high level of conserved residues in this region and the number of FALS-related Cu_2Zn_2SOD mutants found within, it is readily apparent that the disruption of this critical region of the protein plays a significant role in the creation of the pathological properties associated with Cu_2Zn_2SOD mutants.

The pathological mechanism of FALS-associated Cu_2Zn_2-SOD mutants remains an elusive target. However, it is becoming clearer that discrete structural instability and dynamic properties of these mutants are likely to play an essential role in the etiology of the disease. In this study, we have presented convincing evidence that G93A Cu_2Zn_2-SOD displays dynamic and structural characteristics not present in the wild-type protein, which undoubtedly contribute to the pathology of FALS-related Cu_2Zn_2SOD. Further studies are being carried out to gain more insight into how these distinct characteristics of G93A Cu_2Zn_2SOD selectively affect motor neurons at advanced stages of life.

ACKNOWLEDGMENT

We kindly thank Dr. Fiorenza Cramaro for the help in the spectra assignment along with Amir Liba, Bryan Shaw, and Jorge Rodrigue for their help with ICP, MS, and DSC analysis. Professor Daryl Eggers, Professor John Hart, and

Dr. Aram Nersissian are also acknowledged for their insightful comments.

SUPPORTING INFORMATION AVAILABLE

Examples of ^{15}N R_1 and R_2 relaxation data (Figure 1) and R_1, R_2, and NOE values of G93A Cu_2Zn_2SOD (Figure 2). This material is available free of charge via the Internet at http://pubs.acs.org.

REFERENCES

1. Adams, R. D., Vinctor, M., and Ropper, A. H. (1998) in *Principles of neurology*, McGraw-Hill Health Professions Division, New York.
2. Rosen, D. R., Siddique, T., Patterson, D., Figlewicz, D. A., Sapp, P., Hentati, A., Donaldson, D., Goto, J., O'Regan, J., Deng, H. X., Rahmani, Z., Krizus, A., McKenna-Yasek, D., Cayabyab, A., Gatson, S. M., Berger, R., Tanzi, R. E., Halperin, J. J., Herzfeldt, B., Van der Bergh, R., Hung, W.-Y., Bird, T., Deng, G., Mulder, D. W., Smyth, C., Laing, N. G., Soriano, E., Pericak-Vance, M. A., Haines, J., Rouleau, G. A., Gusella, J. S., Horvitz, H. R., and Brown, R. H., Jr. (1993) Mutation in Cu,Zn superoxide dismutase gene are associated with familial amyotrophyc lateral sclerosis, *Nature 362*, 59−62.
3. Deng, H. X., Hentati, A., Tainer, J. A., Lqbal, Z., Cyabyab, A., Hang, W.-Y., Getzoff, E. D., Hu, P., Herzfeldt, B., Roos, R. P., Warner, C., Deng, G., Soriano, E., Smyth, C., Parge, H. E., Ahmed, A., Roses, A. D., Hallewell, R. A., Pericak-Vance, M. A., and Siddique, T. (1993) Amyotrophic lateral sclerosis and structural defects in Cu,Zn superoxide dismutase, *Science 261*, 1047−1051.
4. Elshafey, A., Lanyon, W. G., and Connor, J. M. (1994) Identification of a new missense point mutation in exon 4 of the Cu/Zn superoxide dismutase (SOD-1) gene in a family with amyotrophic lateral sclerosis, *Hum. Mol. Genet. 3*, 363−364.
5. Esteban, J., Rosen, D. R., Bowling, A. C., Sapp, P., McKenna-Yasek, D., O'Regan, J. P., Beal, M. F., Horvitz, H. R., and Brown, R. H. J. (1994) Identification of two novel mutations and a new polymorphism in the gene for Cu/Zn superoxide dismutase in patients with amyotrophic lateral sclerosis, *Hum. Mol. Genet. 3*, 997−998.
6. Borchelt, D. R., Lee, M. K., Slunt, H. S., Guarnieri, M., Xu, Z. S., Wong, P. C., Brown, R. H., Price, D. L., Sisodia, S. S., and Cleveland, D. W. (1994) Superoxide dismutase 1 with mutations linked to familial amyotrophic lateral sclerosis possesses significant activity, *Proc. Natl. Acad. Sci. U.S.A. 91*, 8292−8296.
7. Gurney, M. E., Pu, H., Chiu, A. Y., Dal Canto, M., Polchow, C. Y., Alexander, D. D., Caliendo, J., Hentati, A., Kwon, Y. W., Deng, H. X., Chen, W., Zhai, P., Sufit, R., and Siddique, T. (1994) Motor Neuron Degeneration in Mice That Express a Human Cu,Zn Superoxide Dismutase Mutation, *Science 264*, 1772−1775.
8. Reaume, A. G., Howland, D. S., Trusko, S. P., Savage, M. J., Lang, D. M., Greenberg, B. D., Siman, R., and Scott, R. W. (1996) Motor neurons in Cu/Zn superoxide dismutase-deficient mice develop normally but exhibit enhanced cell death after axonal injury, *Nat. Genet. 13*, 43−47.
9. Valentine, J. S., and Pantoliano, M. W. (1981) in *Copper Proteins* (Spiro, T. G., Ed.) pp 291, Wiley, New York.
10. Fridovich, I. (1995) Superoxide radical and Superoxide dismutases, *Annu. Rev. Biochem. 64*, 97−112.
11. Tainer, J. A., Getzoff, E. D., Richardson, J. S., and Richardson, D. C. (1983) Structure and Mechanism of Copper, Zinc Superoxide Dismutase, *Nature 306*, 284−287.
12. Parge, H. E., Hallewell, R. A., and Tainer, J. A. (1992) Atomic structures of wild-type and thermostable mutant recombinant human Cu,Zn superoxide dismutase, *Proc. Natl. Acad. Sci. U.S.A. 89*, 6109−6114.
13. Hallewell, R. A., Imlay, K. C., Laria, I., Gallegos, C., Fong, N. M., Irvine, B., Cabelli, D. E., Bielski, B. H. J., Olson, P., Mullenbach, G. T., and Cousens, L. S. (1991) Thermostabilization of recombinant CuZn superoxide dismutases by replacement of free cysteines, *Biochem. Biophys. Res. Commun. 181*, 474−480.
14. Hayward, L. J., Rodriguez, J. A., Kim, J. W., Tiwari, A., Goto, J. J., Cabelli, D. E., Valentine, J. S., and Brown, R. H. J. (2002) Decreased metallation and activity in subsets of mutant superoxide dismutases associated with familial ALS, *J. Biol. Chem. 277*, 15923−15931.
15. Rodriguez, J. A., Valentine, J. S., Eggers, D. K., Roe, J. A., Tiwari, A., Brown, R. H. J., and Hayward, L. J. (2002) Familial ALS-associated mutations decrease the thermal stability of distinctly metallated species of human copper−zinc superoxide dismutase, *J. Biol. Chem. 277*, 15923−15931.
16. Hart, P. J., Liu, H., Pellegrini, M., Nersissian, A. M., Gralla, E. B., Valentine, J. S., and Eisenberg, D. (1998) Subunit asymmetry in the three-dimensional structure of a human CuZnSOD mutant found in familial amyotrophic lateral sclerosis, *Protein Sci. 7*, 545−555.
17. Banci, L., Bertini, I., Cramaro, F., Del Conte, R., Rosato, A., and Viezzoli, M. S. (2000) Backbone Dynamics of Human Cu, Zn Superoxide Dismustase and of its Monomeric F50/EG51E/E133Q Mutant: The influence of Dimerization on Mobility and Function, *Biochemistry 39*, 9108−9118.
18. Getzoff, E. D., Tainer, J. A., Stempien, M. M., Bell, G. I., and Hallewell, R. A. (1989) Evolution of CuZn superoxide dismutase and the greek key β-barrel structural motif, *Proteins: Struct., Funct., Genet. 5*, 322−336.
19. de Belleroche, J., Orrell, R. W., and Virgo, L. (1996) Amyotrophic lateral sclerosis: recent advances in understanding disease mechanisms, *J. Neuropathol. Exp. Neurol. 55*, 747−757.
20. Getzoff, E. D., Cabelli, D. E., Fisher, C. L., Parge, H. E., Viezzoli, M. S., Banci, L., and Hallewell, R. A. (1992) Faster Superoxide Dismutase Mutants Designed by Enhancing Electrostatic Guidance, *Nature 358*, 347−351.
21. Lepock, J. R., Frey, H. E., and Hallewell, R. A. (1990) Contribution of conformational stability and reversibility of unfolding to the increased thermostability of human and bovine superoxide dismutase mutated at free cysteines, *J. Biol. Chem. 265*, 21612−21618.
22. Banci, L., Bertini, I., Borsari, M., Viezzoli, M. S., and Hallewell, R. A. (1995) Mutation of the metal bridging-proton donor His 63 residue in human Cu,Zn superoxide dismutase: biochemical and biophysical analysis of the His 63 to Cys mutant, *Eur. J. Biochem. 232*, 220−225.
23. Farrow, N. A., Muhandiram, R., Singer, A. U., Pascal, S. M., Kay, C. M., Gish, G., Shoelson, S. E., Pawson, T., Forman-Kay, J. D., and Kay, L. E. (1994) Backbone dynamics of a free and phosphopeptide-complexed Src homology 2 domain studied by ^{15}N NMR relaxation, *Biochemistry 33*, 5984−6003.
24. Wang, A. C., and Bax, A. (1993) Minimizing the effects of radio-frequency heating in multidimensional NMR experiments, *J. Biomol. NMR 3*, 715−720.
25. Tjandra, N., Wingfield, P., Stahl, S., and Bax, A. (1996) Anisotropic rotational diffusion of perdeuterated HIV protease from ^{15}N NMR relaxation measurements at two magnetic fields, *J. Biomol. NMR 8*, 273−284.
26. Mulder, F. A., Van Tilborg, P. J., Kaptein, R., and Boelens, R. (1999) Microsecond time scale dynamics in the RXR DNA-binding domain from a combination of spin-echo and off-resonance rotating frame relaxation measurements, *J. Biomol. NMR 13*, 275−288.
27. Grzesiek, S., and Bax, A. (1993) The importance of not saturating H_2O in protein NMR. Application to sensitivity enhancement and NOE measurements, *J. Am. Chem. Soc. 115*, 12593−12594.
28. Meiboom, S., and Gill, D. (1960) Modified spin-echo method for measuring nuclear relaxation times, *Rev. Sci. Instr. 29*, 688−691.
29. Zinn-Justin, S., Berthault, P., Guenneugues, M., and Desvaux, H. (1997) Off-resonance RF fields in heteronuclear NMR. Application to the study of slow motions, *J. Biomol. NMR 10*, 363−372.
30. Desvaux, H., Berthault, P., Birlirakis, N., Goldman, M., and Piotto, M. (1995) Improved versions of Off-Resonance ROESY, *J. Magn. Reson. 113*, 47−52.
31. Marquardt, D. W. (1963) An algorithm for least-squares estimation of nonlinear parameters, *J. Soc. Ind. Appl. Math. 11*, 431−441.
32. Press, W. H., Flannery, B. P., Teukolsky, S. A., and Vetterling, W. T. (1988) in *Numerical Recipes in C: The Art of Scientific Computing*, Cambridge University Press, New York.
33. Peng, J. W., and Wagner, G. (1992) Mapping of the spectral densities of N−H bond motions in eglin c using heteronuclear relaxation experiments, *Biochemistry 31*, 8571−8586.
34. Desvaux, H., Birlirakis, N., Wary, C., and Berthault, P. (1995) Study of slow molecular motions in solution using off-resonance irradiation in homonuclear NMR. II. Fast chemical exchange processes, *Mol. Phys. 86*, 1059−1073.

35. Akke, M., and Palmer, A. G., III (1996) Monitoring macromolecular motions on microsecond to millisecond time scales by $R_{1\rho}$-R_1 constant relaxation time NMR spectroscopy, *J. Am. Chem. Soc. 118*, 911−912.
36. Szyperski, T., Luginbuhl, P., Otting, G., Güntert, P., and Wüthrich, K. (1993) Protein dynamics studied by rotating frame ^{15}N spin relaxation times, *J. Biomol. NMR 3*, 151−164.
37. Lipari, G., and Szabo, A. (1982) Model-Free approach to the interpretation of nuclear magnetic resonance relaxation in macromolecules. 1. Theory and range of validity, *J. Am. Chem. Soc. 104*, 4546−4559.
38. Clore, G. M., Szabo, A., Bax, A., Kay, L. E., Driscoll, P. C., and Gronenborn, A. M. (1990) Deviations from the simple two-parameter model-free approach to the interpretation of nitrogen-15 nuclear magnetic relaxation of proteins, *J. Am. Chem. Soc. 112*, 4989−4991.
39. Abragam, A. (1961) in *The Principles of Nuclear Magnetism*, Oxford University Press, Oxford, U.K.
40. Mandel, M. A., Akke, M., and Palmer, A. G., III (1995) Backbone dynamics of *Escherichia coli* ribonuclease HI: correlations with structure and function in an active enzyme, *J. Mol. Biol. 246*, 144−163.
41. Luginbuhl, P., Pervushin, K. V., Iwai, H., and Wüthrich, K. (1997) Anisotropic molecular rotational diffusion in ^{15}N spin relaxation studies of protein mobility, *Biochemistry 36*, 7305−7312.
42. Woessner, D. E. (1962) *J. Chem. Phys. 3*, 647−652.
43. Lee, L. K., Rance, M., Chazin, W. J., and Palmer, A. G., III (1997) Rotational diffusion anisotropy of proteins from simultaneous analysis of ^{15}N and ^{13}C alpha nuclear spin relaxation, *J. Biomol. NMR 9*, 287−298.
44. Brüschweiler, R., Liao, X., and Wright, P. E. (1995) Long-range motional restrictions in a multidomain zinc-finger protein from anisotropic tumbling, *Science 268*, 886−889.
45. Stone, M. J. (2001) NMR Relaxation Studies of the Role of Conformational Entropy in Protein Stability and Ligand Binding, *Acc. Chem. Res. 34*, 379−388.
46. Yang, D., and Kay, L. E. (1996) Contributions to Conformational Entropy Arising from Bond Vector Fluctuations Measured from NMR-Derived Order Parameters: Application to Protein Folding, *J. Mol. Biol. 263*, 369−382.
47. Bartels, C., Güntert, P., Billeter, M., and Wüthrich, K. (1997) GARANT: A General Algorithm for Resonance Assignment of Multidimensional Nuclear Magnetic Resonance Spectra, *J. Comput. Chem. 18*, 139−149.
48. Banci, L., Bertini, I., Cramaro, F., Del Conte, R., and Viezzoli, M. S. (2002) The solution structure of reduced dimeric copper zinc SOD: the structural effects of dimerization, *Eur. J. Biochem. 269*, 1905−1915.
49. Palmer, A. G., III, Williams, J., and McDermott, A. (1996) Nuclear Magnetic Resonance Studies of Biopolymer Dynamics, *J. Phys. Chem. 100*, 13293−13310.
50. Hodsdon, M. E., and Cistola, D. P. (1997) Ligand binding alters the backbone mobility of intestinal fatty acid-binding protein as monitored by ^{15}N NMR relaxation and ^{1}H exchange, *Biochemistry 36*, 2278−2290.
51. Deng, H. X., Tainer, J. A., Mitsumoto, H., Ohnishi, A., He, X., Hung, W. Y., Zhao, Y., Juneja, T., Hentati, A., and Siddique, T. (1995) Two novel SOD1 mutations in patients with familial amyotrophic lateral sclerosis, *Hum. Mol. Genet. 4*, 1113−1116.
52. Banci, L., Felli, I. C., and Kummerle, R. (2002) Direct detection of hydrogen bonds in monomeric superoxide dismutase: biological implications, *Biochemistry 41*, 2913−2920.
53. Palmer, A. G., III, Cavanagh, J., Wright, P. E., and Rance, M. (1991) Sensitivity improvement in proton-detected two dimensional heteronuclear correlation NMR spectroscopy, *J. Magn. Reson. 93*, 151−170.
54. Arnesano, F., Banci, L., Barker, P. D., Bertini, I., Rosato, A., Su, X. C., and Viezzoli, M. S. (2002) *Biochemistry 41*, 13587−13594.
55. Lyons, T. J., Nerissian, A., Huang, H., Yeom, H., Nishida, C. R., Graden, J. A., Gralla, E. B., and Valentine, J. S. (2000) The metal binding properties of the zinc site of yeast copper−zinc superoxide dismutase: implications for amyotrophic lateral sclerosis, *J. Biol. Inorg. Chem. 5*, 189−203.
56. Crow, J. P., Sampson, J. B., Zhuang, Y., Thomson, J. A., and Beckman, J. S. (1997) Decreased zinc affinity of amyotrophic lateral sclerosis-associated superoxide dismutase mutants leads to enhanced catalysis of tyrosine nitration by peroxynitrite, *J. Neurochem. 69*, 1936−1944.
57. Lyons, T. J., Liu, H., Goto, J. J., Nerissian, A., Roe, J. A., Graden, J. A., Café, C., Ellerby, L. M., Bredesen, D. E., and Gralla, E. B. (1996) Mutations in copper−zinc superoxide dismutase that cause amyotrophic lateral sclerosis alter the zinc binding site and the redox behaviour of the protein, *Proc. Natl. Acad. Sci. U.S.A. 93*, 12240−12244.
58. Bruijn, L. I., Houseweart, M. K., Kato, S., Anderson, K. L., Anderson, S. D., Ohama, E., Reaume, A. G., Scott, R. W., and Cleveland, D. W. (1998) Aggregation and motor neuron toxicity of an ALS-linked SOD1 mutant independent from wild-type SOD1, *Science 281*, 1851−1854.
59. Johnston, J. A., Dalton, M. J., Gurney, M. E., and Kopito, R. R. (2000) Formation of high molecular weight complexes of mutant Cu, Zn-superoxide dismutase in a mouse model for familial amyotrophic lateral sclerosis, *Proc. Natl. Acad. Sci. U.S.A. 97*, 12571−12576.
60. Richardson, J. S., and Richardson, D. C. (2002) Natural β-sheet proteins use negative design to avoid edge-to-edge aggregation, *Proc. Natl. Acad. Sci. U.S.A. 99*, 2754−2759.
61. Garrett, D. S., Seok, Y. J., Liao, D. I., Peterkofsky, A., Gronenborn, A. M., and Clore, G. M. (1997) N-terminal domain of enzyme I of the *Escherichia coli* phosphoenolpyruvate:sugar phosphotransferase system by multidimensional NMR, *Biochemistry 36*, 2517−2530.

BI026704Y